DEM-Assisted 3-D Reconstruction of Aletsch Glacier Displacements Using Monostatic and Bistatic Differential Interferometry

Esther Mas Sanz, *Member, IEEE*, Marcel Stefko, *Member, IEEE*, and Irena Hajnsek, *Fellow, IEEE*

***Abstract*— Differential interferometry is a powerful remote sensing technique that allows radar systems to capture very small displacements from a far observational position. Most systems are monostatic, meaning that they can only capture displacement changes in the line of sight (LOS). The simplicity of monostatic systems also restricts their suitability to either displacements with a single principal motion direction or with a known direction in space. Adding a passive receiver (bistatic systems) provides an additional LOS of information, allows to reconstruct more complex vector fields, and reduces the assumptions on the displacement direction. This study presents a set of differential interferometric observations retrieved in the Aletsch glacier during a winter campaign in March 2022, using Ku-band Advanced Polarimetric Radar Interferometer (KAPRI), a Ku-band ground-based radar interferometer. We investigate the glacier motion based on the datasets corresponding to each of KAPRI's configurations and propose two independent approaches to solve the displacement field: monostatic (1 LOS) and monostatic–bistatic (2 LOS). As the monostatic and bistatic datasets were retrieved simultaneously, it is possible to do a direct comparison of the resulting displacements and the respective uncertainties. Results show that the accumulated displacement for the 09:01:30 h to 10:13:30 h at the near-range region (ROI 1) is 3.83 mm in the monostatic case and 4.42 mm in the monostatic–bistatic case. In the far-range region (ROI 3), the monostatic displacements result in 8.54 mm while according to the bistatic approach 17.82 mm. Assumptions used for the monostatic resolution of the glacier displacements hold for the flatter areas corresponding to the main glacier flow but fail in the steep terrain. Monostatic acquisitions present a high signal-to-noise ratio (SNR), which maintains a low uncertainty [below 0.5 mm for all regions of interest (ROIs)] throughout the scene compared to the bistatic dataset. Monostatic–bistatic derived displacements are susceptible to the increased noise in the far range but yield a more robust (direction and magnitude) and smoother displacement field in the near-mid range. These comparisons provide valuable insights on the advantages and shortcomings of employing monostatic and bistatic configurations for 3-D displacement retrieval and serve as proxy for upcoming satellite missions that plan to use bistatic radar configurations.**

***Index Terms*— Bistatic radar, differential interferometry, glacier displacements.**

Received 3 February 2025; revised 26 May 2025; accepted 18 June 2025. Date of publication 7 July 2025; date of current version 21 July 2025. *(Corresponding author: Esther Mas Sanz.)*

Esther Mas Sanz and Marcel Stefko are with the Chair of Earth Observation and Remote Sensing, Institute of Environmental Engineering, ETH Zürich, 8093 Zürich, Switzerland (e-mail: esmasi@ethz.ch).

Irena Hajnsek is with the Chair of Earth Observation and Remote Sensing, Institute of Environmental Engineering, ETH Zürich, 8093 Zürich, Switzerland, and also with the Microwaves and Radar Institute, German Aerospace Center, 82234 Weßling, Germany.

Digital Object Identifier 10.1109/TGRS.2025.3586272

I. INTRODUCTION

A. Principles of Differential Interferometry

DIFFERENTIAL interferometry is a widespread radar remote sensing technique that exploits signal phase differences between two (or more) radar images that result from varying the temporal baseline of the acquisitions [1]. These phase shifts are sensitive to variations of the order of magnitude of the wavelength, thus allowing radar systems to detect very small displacements (in some cases submillimeter level) compared to the observation distance (in the order of kilometers). Adjusting the temporal baseline will determine the dynamism of the captured movements, ranging from phenomena changing few millimeters within the span of months [2] to highly dynamic phenomena such as ice flow dynamics at the terminus of a glacier [3].

Depending on the requirements of the acquisition, different radar platforms can be used, namely, space, airborne, and ground-based systems. Within the context of differential interferometry, one of the main drawbacks of airborne and satellite systems is their limited repeating times, with revisit times of at least 6–12 days in the case of satellite systems and the order of tenths of minutes for airborne ones [4], [5]. Therefore, acquiring high-density temporal data during extended periods of time poses a serious challenge. This fact combined with the high costs and logistic complexity of these missions makes ground-based systems a suitable choice, in particular, to test new concepts when large swaths are not required.

B. Types of Radar Systems: Monostatic and Bistatic

Most ground-based radar differential interferometry studies use standalone monostatic systems [6]. In other words, interferometric radar images are obtained at a specific time by a single radar with transmitting and receiving antennas placed in the same position. Although this configuration presents clear advantages in terms of simplicity for instrument design, deployment, and data processing, as well as reduced costs and logistical challenges, the recovered information can only provide displacements in one direction. Indeed, the variations in the interferometric phase solely describe changes along the line of sight (LOS). Such a configuration is ideal for monitoring displacements that often are assumed to have one principal motion of direction, such as in the case of terrain subsidence [7] or landslides (see [8], the displacement motion is at least 60% along the LOS). For solving displacements that have 2-D motion, an additional independent LOS is necessary to solve the two directions and create a vector field. This can be achieved by simply adding another standalone monostatic system [9], [10]. However, this solution is rather costly and often impractical. Hence, instead of relying on an extra deployed monostatic sensor, it is also possible to employ a secondary receiver at a location different than the transmitting platform. For the purposes of this article, configurations involving a monostatic system with a passive receiver in a different location will be referred to as a "bistatic system." However, it should be noted that there are a number of ways to define a bistatic radar configuration and its particular definition is application dependent [11]. For example, in [12], a ground-based synthetic aperture radar (SAR) is combined together with a transponder to detect two displacement components of a nearby corner reflector. Later, the same authors use the monostatic–bistatic interferometric radar to monitor the 2-D displacements of man-made slander structures such as telecommunication towers [13]. Despite not being bistatic *sensu stricto*, other investigations involve the simultaneous operation of three radars to measure the small 3-D displacements of a corner reflector [14], [15], [16] or full-field microdeformations of the scene by the addition of a fourth one in order to reduce errors [17]. The investigations performed in [18] use a purely bistatic approach combining a single radar and two transponders to estimate bridge displacements, and in [19], a similar goal is achieved by the use of multiple-input–multiple-output radars.

C. Importance of Glacier Monitoring

As the examples listed in Section I-B, most ground-based radar investigations focus either on landslide monitoring or on displacement retrieval of man-made structures (e.g., buildings, bridges, towers, and chimneys), whereas only a small share target glaciers [6]. The amount of studies becomes even narrower if accounting for glacier investigations using ground-based bistatic systems, most likely, due to the technical and logistical difficulties associated with these remote regions. We find only one example, in [10], in which two synchronized and identical terrestrial radar interferometers (TRIs) are deployed a few hundreds of meters apart. With this configuration, they are able to construct a glacier velocity assumed to be contained in the LOS plane defined by the two devices.

The relevance of glacier investigations using bistatic systems is twofold. First, because the monitoring of glaciers is paramount to understand cryospheric processes and their role in Earth's climate [20]. Second, because glaciers together with ice sheets, snow-covered areas constitute the main interest targets in current [5] and future [21], [22], [23] spaceborne bistatic missions. Furthermore, the fact that transmitting and receiving antennas are placed in different positions opens possibilities beyond differential interferometry. Indeed, it allows to explore specific scattering phenomena that rely on different signal paths for transmission and reception legs, such as the coherent backscatter opposition effect (CBOE) [24], and brings out geometrical and physical properties about the structure of the target inaccessible to the only-monostatic mode [25]. Therefore, ground-based bistatic systems serve as proxies by exploring bistatic-specific challenges in glacier regions.

D. Contributions of This Article

In this study, a monostatic–bistatic ground-based radar is used to reconstruct the 3-D displacements of the Jungfraujoch region (Aletsch glacier). The particular geometry of the scene invalidates the assumption that the glacier displacements are contained within the LOS plane of the two devices nor that displacements are strictly 2-D. Following the approach in [26], the glacier displacement is modeled as a 3-D displacement vector, which is constructed using two different methodologies for the purely monostatic acquisitions (1 LOS) and the monostatic–bistatic ones (2 LOS).

The contributions from this article are given as follows.

1) Developing two methods for the calculation of the 3-D displacements of a glacier. A monostatic method in which the direction is given by an external digital elevation model (DEM). A monostatic–bistatic method, in which the external DEM imposes the flow direction to be parallel to the glacier surface.
2) Analyzing the displacement's uncertainty based on the analytical derivation of uncertainty propagation, which includes the effects of signal-to-noise ratio (SNR). A numerical approach to estimate precision loss in the monostatic–bistatic case, without including the effects of SNR.
3) Discussing and comparing the displacements obtained by the monostatic and monostatic–bistatic methods and the shortcomings and advantages of each method.

This article is organized as follows. Section II describes the two different approaches to reconstruct the glacier displacements. Section III provides a description of the instrument and the experimental setup utilized during the campaign. Section IV describes the dataset and campaign specifics. Section V presents the results, namely, the displacement fields obtained using the monostatic and monostatic–bistatic approaches and the uncertainty maps. A discussion of the results is given in Section VI. Finally, Section VII concludes this article.

II. 3-D Displacement Reconstruction

In this section, we present two different approaches to reconstruct the 3-D displacements of the glacier: one that relies on the monostatic acquisitions only (monostatic formulation) and another that combines the monostatic and bistatic data (monostatic–bistatic formulation). The first is based on the phase variations observed in a single LOS, while the second approach employs two independent LOS for these phase variations. In addition to the monostatic and bistatic radar datasets (detailed in Section III), we also work with a light detection and ranging (LiDAR)-derived DEM obtained from SwissALTI3D©. Both the monostatic and bistatic datasets share most of the processing steps, which are a combination of using the GAMMA software package and use-case specific

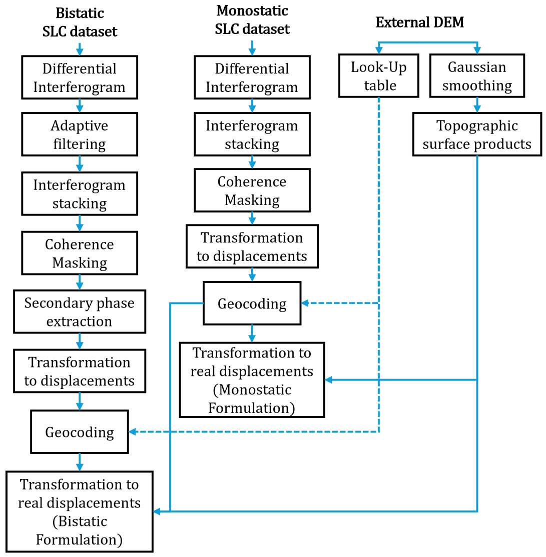

Fig. 1. Diagram of the processing pipeline for the displacement calculation using the monostatic and monostatic–bistatic approaches.

Python scripts managed by a Nextflow pipeline [27]. Fig. 1 shows a schematic description of the processing pipeline followed.

Single-look complex (SLC) files are used to produce differential interferograms of approximately 2-min temporal baseline and spatially averaged with a multilook window of 5 × 1 (range × azimuth averaged pixels). Only the bistatic differential interferograms, due to their lower SNR, are filtered using the adaptive filter algorithm in [28]. Relying on the fact that the displacements are sufficiently small so that the differential phase remains between the values of $-\pi$ and π (see [29, Fig. 3.7]), interferograms are stacked from the initial to the final acquisition time. This results in two stacked interferograms: one for the monostatic dataset and another for the bistatic dataset. The stacked interferograms are masked using a coherence mask with thresholds 0.7 for the monostatic and 0.6 for the bistatic case. The following step consists of transforming the accumulated phase to the LOS displacement. In the case of the monostatic differential interferometric case, it is quite straightforward. The following formula describes how an arbitrary interferometric phase is obtained after a small change in range in the transmission (ΔR_T) and reception (ΔR_R) legs:

$$\Delta\phi = \frac{2\pi}{\lambda}(\Delta R_T + \Delta R_R). \tag{1}$$

More commonly seen in literature for the monostatic case

$$\Delta\phi_m = \frac{4\pi}{\lambda}\Delta R_T \tag{2}$$

as the transmission and reception legs are the same, $\Delta R_T = \Delta R_R$. For the bistatic case, we use (1) and substitute the transmission leg by (2); the bistatic phase $\Delta\phi_b$ could be expressed as

$$\Delta\phi_b = \frac{2\pi}{\lambda}\Delta R_T + \frac{2\pi}{\lambda}\Delta R_R = \frac{\Delta\phi_m}{2} + \frac{2\pi}{\lambda}\Delta R_R \tag{3}$$

in which it is divided into a contribution on the transmitting leg equal to half of the monostatic phase and another belonging to the reception leg. The latter can be defined as the secondary interferometric phase

$$\Delta\phi_s = \frac{2\pi}{\lambda}\Delta R_R. \tag{4}$$

In other words, the differential interferometric phase of the bistatic acquisitions only contains new information of the displacement—with respect to the monostatic—in the secondary phase contribution. Thus, the secondary phase (4) is isolated in order to calculate the LOS displacements of the bistatic receiver. The final step is calculating the displacement vector $\vec{s}$, the actual displacement vector that describes the motion of the target in 3-D space, from the LOS displacement values. To do so, it is necessary to geocode the LOS displacements as well as a series of derived products that describe the terrain's topography. An external DEM is used to generate the geocoding lookup table, to obtain a grid of coordinates, and the gradient and surface normal vectors. The DEM is smoothed using a Gaussian filter in order to remove spatially high gradient variations that do not correspond to surface topography but to features of the terrain captured in the DEM (e.g., crevasses, surface roughness, and stones). The data processing differs whether using the monostatic data (monostatic formulation, see Section II-A) or the monostatic transmitter and the bistatic receiver one (monostatic–bistatic method, see Section II-B).

A. Monostatic Formulation

The displacement vector $\vec{s}$ is modeled as a 3-D vector that when projected on the LOS of the primary radar device results in the LOS displacement value [Fig. 2(a)]. It can be expressed as

$$\vec{s} \cdot \vec{u}_m = \Delta R_T \tag{5}$$

where $\vec{u}_m$ is the LOS vector for the monostatic (transmitting and receiving) device. As only the monostatic dataset is used to calculate the displacements, there are three degrees of freedom (DOFs) unrestricted on (5). In order to restrict the 3-D vector direction and ensure uniqueness in the solution, an external DEM is needed. If we take $z(x, y)$ as the terrain topography and $\nabla_{\text{surface}} z(x, y)$ as the 3-D gradient vector of the parametrized surface, then (6) expresses the normalized 3-D vector of the surface

$$\hat{g} = \frac{\nabla_{\text{surface}} z(x, y)}{||\nabla_{\text{surface}} z(x, y)||}. \tag{6}$$

Next, we impose the direction of $\hat{g}$ to the direction of the displacement vector

$$\vec{s} = ||\vec{s}|| \cdot \hat{g}. \tag{7}$$

Hence, the only unknown remaining is the magnitude of the displacement, which can be directly computed

$$||\vec{s}|| = \frac{\lambda}{4\pi\left(\hat{g} \cdot \vec{u}_m\right)}\Delta\phi_m. \tag{8}$$

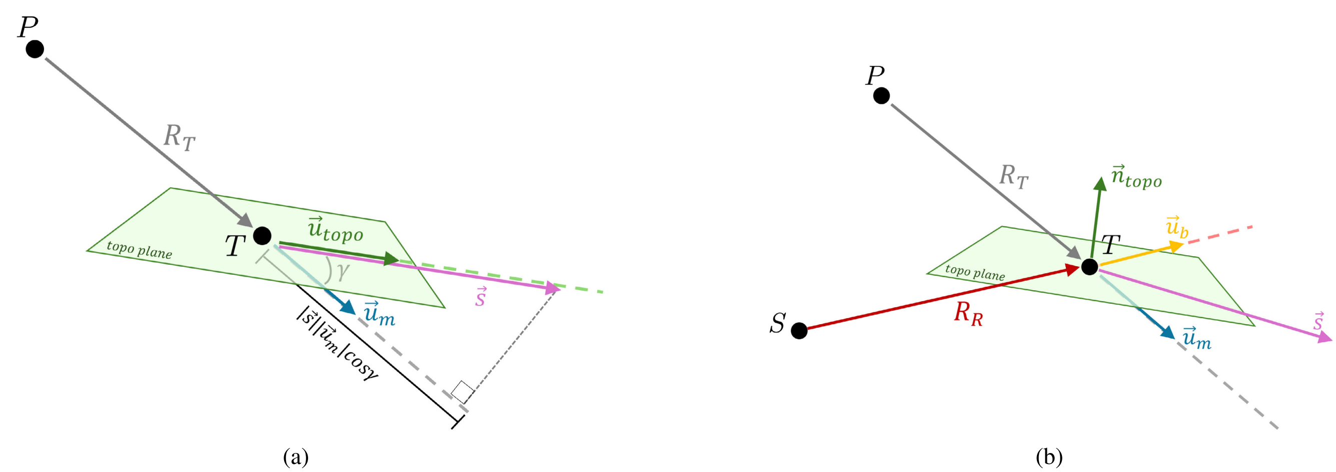

Fig. 2. Displacements diagrams. (a) Diagram of the monostatic displacements. P and T refer to the primary device and target, respectively. The gradient of the topography is $\hat{g}$, the unitary LOS of the primary device is $\overrightarrow{u}_m$, and the angle between them is γ. The displacement vector $\overrightarrow{s}$ has the same direction as the gradient of the topography, and its projection on the LOS (dot product) corresponds to the differential interferometric phase. (b) Diagram of the bistatic displacements. S refers to the secondary device. The unitary vector of the bistatic LOS is $\overrightarrow{u}_b$ and the unitary normal vector of the tangent plane to the topography is $\overrightarrow{n}_t$. The displacement vector $\overrightarrow{s}$ is displayed as an arbitrary vector perpendicular to $\overrightarrow{n}_t$.

B. Monostatic–Bistatic Formulation

Mirroring (5), the LOS displacements associated with the secondary phase can be expressed as a projection of the real 3-D displacement vector on the bistatic LOS vector

$$\overrightarrow{s} \cdot \overrightarrow{u}_b = \Delta R_R \tag{9}$$

where $\overrightarrow{u}_b$ is the LOS vector for the bistatic (passive receiver) device. To calculate the bistatic displacements, the system of equations composed by (5) and (9) is used. However, these two equations still have 1 DOF, resulting in an infinity of mathematically possible solutions. Therefore, an additional assumption is imposed based on a geometrical restriction: the displacement vector is assumed to be contained in the tangent plane to the topography

$$\vec{s} \cdot \vec{n}_t = 0 \tag{10}$$

where $\overrightarrow{n_t}$ is the normal vector of the aforementioned plane. Physically, (10) translates to displacements that will only be tangent to the terrain's surface, thus not being a valid solution for ground subsidence (soil downward motion) or heave (upward motion). This approximation leads to displacement that will be contained in the same plane as those calculated using monostatic data only (monostatic method) but will allow their direction to differ from the gradients.

C. Propagation of Uncertainty

According to the propagation of uncertainty theory [30], given an output quantity Y expressed in terms of a series of independent quantities $X_1, X_2, X_3 \ldots, X_n$ as

$$Y = f(X_1, X_2, X_3, \ldots, X_n). \tag{11}$$

Its squared standard uncertainty can be expressed as

$$\sigma_Y^2 = \sum_{i=1}^{n} \sigma_{X_i}^2 \left(\frac{\partial Y}{\partial X_i}\right)^2 \tag{12}$$

assuming that the covariance terms between all input quantities $(X_1, X_2, \ldots)$ are zero (input quantities are independent) and that Y can be expressed as a first-order approximation in the vicinity of the evaluated point to calculate the uncertainty.

In the case of monostatic displacement calculation, the standard uncertainty estimation is expressed as:

$$\sigma_{||s||} = \frac{\lambda}{4\pi\left(\hat{g} \cdot \overrightarrow{u}_m\right)} \sigma_{\phi_m} \tag{13}$$

where $\hat{g}$ is the gradient of the surface topography and $\overrightarrow{u}_m$ the LOS vector from the primary device. According to [31] and [32], the uncertainty of the phase can be obtained by using an approximation relating it to the SNR

$$\sigma_\phi = \frac{1}{\sqrt{\mathrm{SNR}}}. \tag{14}$$

In case of the bistatic displacements, the formulation presents a slightly higher complexity to derive the displacement's uncertainty. The linear system presented in (5), (9), and (10) can be expressed explicitly as

$$\begin{cases} s_x \cdot u_{m_x} + s_y \cdot u_{m_y} + s_z \cdot u_{m_z} = \dfrac{\lambda}{4\pi}\phi_m \\ s_x \cdot u_{b_x} + s_y \cdot u_{b_y} + s_z \cdot u_{b_z} = \dfrac{\lambda}{2\pi}\phi_s \\ s_x \cdot n_x + s_y \cdot n_y + s_z \cdot n_z = 0 \end{cases} \tag{15}$$

where $< x, y, z >$ are the easting, northing, and height components of an orthonormal base with origin on the primary radar device. Intuitively, the uncertainty of the magnitude of the displacement will be a function of the uncertainties of the differential interferometric phases ϕ_P and ϕ_S as well as dependent on the geometrical configuration between $\overrightarrow{u}$ and $\overrightarrow{v}$ (expressed by β) and with respect to the normal $\overrightarrow{n}$.

While the $< x, y, z >$ base is convenient to use in numerical computations, it becomes a disadvantage when isolating the components of $\overrightarrow{s}$ and expressing its magnitude as a function of the independent variables. Relying on the invariance of the

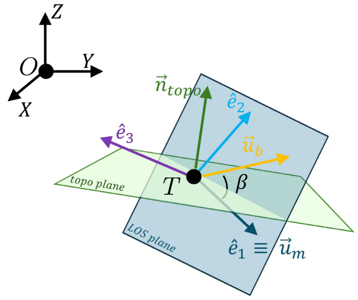

Fig. 3. Diagram with global base $< x, y, z >$ (easting, northings, and height) and orthonormal local base system $< \hat{e}_1, \hat{e}_2, \hat{e}_3 >$. The $\hat{e}_1$-direction corresponds to the monostatic LOS direction, $\hat{e}_3$ is the vector product of the monostatic and bistatic LOS directions, and $\hat{e}_2$ completes the orthonormal base. The angle β refers to the angle between the monostatic and bistatic LOS directions.

modulus of a vector and the dot product irrespective of their base, a change to a local base is performed in order to analyze the uncertainty propagation formula.

The local base is constructed as follows. Let $\hat{e}_1$ be a unitary vector with the direction of the monostatic LOS vector $\overrightarrow{u}$. Let $\hat{e}_3$ be the unitary orthogonal vector be the plane formed by the LOS vectors $\overrightarrow{u}_m$ and $\overrightarrow{u}_b$ calculated as

$$\hat{e}_3 = \frac{\overrightarrow{u}_m \times \overrightarrow{u}_b}{||\overrightarrow{u}_m \times \overrightarrow{u}_b||} \tag{16}$$

and $\hat{e}_2$ as the vector completing the right-handed system $\hat{e}_1$–$\hat{e}_3$ with

$$\hat{e}_2 = \frac{\hat{e}_3 \times \hat{e}_1}{||\hat{e}_3 \times \hat{e}_1||}. \tag{17}$$

In this new base $< \hat{e}_1, \hat{e}_2, \hat{e}_3 >$, the linear system of equations in (15) can be rewritten as follows:

$$\begin{cases} s_1 = \dfrac{\lambda}{4\pi}\phi_m \\ s_1 \cdot \cos(\beta) + s_2 \cdot \sin(\beta) = \dfrac{\lambda}{2\pi}\phi_s \\ s_1 \cdot n_1 + s_2 \cdot n_2 + s_3 \cdot n_3 = 0. \end{cases} \tag{18}$$

This base has the particular advantage that the bistatic LOS vector can be expressed exclusively as a function of the angle β (see Fig. 3) and the different components of the displacement vector can be easily isolated

$$s_1 = \frac{\lambda}{4\pi}\phi_m \tag{19}$$

$$s_2 = -\frac{\lambda\cos(\beta)\phi_m}{4\pi\sin(\beta)} + \frac{\lambda\phi_s}{2\pi\sin(\beta)} \tag{20}$$

$$s_3 = -\frac{\lambda n_1\phi_m}{4\pi n_3} + \frac{\lambda n_2\cos(\beta)\phi_m}{4\pi n_3\sin(\beta)} - \frac{\lambda n_2\phi_s}{2\pi\sin(\beta)}. \tag{21}$$

The magnitude of the displacement can be calculated using the formula for the norm of a 3-D vector

$$||\overrightarrow{s}|| = \sqrt{s_1^2 + s_2^2 + s_3^2}. \tag{22}$$

Therefore, the uncertainty propagation will obey the following equation:

$$\sigma_{||s||} = \sqrt{\left(\frac{\partial||\overrightarrow{s}||}{\partial\phi_m}\right)^2 \sigma_{\phi_m}^2 + \left(\frac{\partial||\overrightarrow{s}||}{\partial\phi_s}\right)^2 \sigma_{\phi_s}^2} \tag{23}$$

in which the respective phase uncertainties for the monostatic and the secondary device are estimated according to the formula provided in (14).

Evaluating the magnitude of the displacement from the local base $< \hat{e}_1, \hat{e}_2, \hat{e}_3 >$ allows a direct comparison to the monostatic method. The uncertainty propagation on the bistatic method is clearly affected by two geometrical components, β and n_3 (the component of the normal topographic vector parallel to $\hat{e}_3$). Assuming constant phase uncertainties σ_{ϕ_m} and σ_{ϕ_s}, when $\beta \to 0°$ the uncertainty increases, and at $\beta = 0°$ the assumptions made in (11) and (12) are no longer valid. The reasoning behind is that in case of a zero angle β, $\overrightarrow{u}_m$ and $\overrightarrow{u}_b$ are parallel or collinear, meaning that the set of equations in (15) does no longer constitute three linear independent equations. The case of $n_3 = 0$ indicates that the topographic normal vector is contained within the LOS plane, resulting in a geometrical configuration of the displacement only possible when the value of this one is that of the null displacements.

D. Condition Number

For a function f as described in (11), if we evaluate its behavior at a particular data point $x \in X$, we can talk about a *well-conditioned* problem if a small perturbation of x leads to a small change in f or an *ill-conditioned* problem if some small perturbation in x leads to large changes in f [33]. To measure appropriately the behavior of f, in this study, we use the condition number κ, defined as a relative error magnification factor [34]. A condition number of 1 means that the errors on the data are not being amplified in the solution, whereas a large condition number indicates divergence in the propagation error. A general definition of κ for a function f is [33]

$$\kappa = \lim_{\delta\to 0} \sup_{||\delta x||\leq\delta} \left(\frac{||\delta f||}{||f||} \Big/ \frac{||\delta x||}{||x||}\right). \tag{24}$$

This definition can be directly applied in the monostatic reconstruction of the displacements. Equation (8) is a nonlinear function that, assuming a constant interferometric phase, only depends on the value of its denominator

$$\hat{g} \cdot \overrightarrow{u}_m = |\hat{g}|\,|\overrightarrow{u}_m| \cos\gamma = \cos\gamma \tag{25}$$

which in turn, being the product of the norm of two unitary vectors, only changes with the cosine of the angle they form, γ. Therefore, our f function has the form

$$f = \frac{k}{\cos\gamma} \tag{26}$$

where the value k is a constant. Applying the definition in (24), the condition number for the monostatic formulation can be obtained as

$$\kappa_m = ||\gamma\tan\gamma||. \tag{27}$$

The error propagation in the system of equations in (15) to calculate the bistatic displacements can also be calculated in terms of the condition number of a matrix. Take the system of equations where δb is the error and and δx is the resulting error [34]

$$A(x + \delta x) = b + \delta b. \tag{28}$$

Then, the scale factor $\kappa(A)$ expresses how much a relative change in the right-hand side of the equation (quantity $||\delta b||/||b||$) results in a relative change of the solution ($||\delta x||/||x||$)

$$\frac{||\delta x||}{||x||} \leq \kappa(A)\frac{||\delta b||}{||b||}. \tag{29}$$

Or alternatively, as the multiplication of the spectral norm (square root of the maximum eigenvalue [35]) of A and its inverse

$$\kappa(A) = ||A|| \cdot ||A^{-1}|| \tag{30}$$

where A is explicitly defined as

$$\begin{bmatrix} u_{m_x} & u_{m_y} & u_{m_z} \\ u_{b_x} & u_{b_y} & u_{b_z} \\ n_x & n_y & n_z \end{bmatrix} \tag{31}$$

if the base is set at the origin of the radar. As in the scalar case, an infinite condition number occurs when A cannot be inverted and the problem is ill-posed [34] and it is independent of the base in which A is defined.

In turn, the number of digits of the precision loss can be calculated as follows:

$$C = \log_{10} \kappa(A). \tag{32}$$

The advantage of precision loss over the uncertainty propagation proposed in Section II-C is that it allows a purely geometrical analysis of the problem, independently of the SNR of the scene. In turn, these provide an additional and independent perspective on the error propagation values and help interpret the different contributions as sources of errors.

III. Instrument Description and Experimental Setup

The dataset was acquired using Ku-band Advanced Polarimetric Radar Interferometer (KAPRI), a real-aperture frequency-modulated continuous-wave (FMCW) radar operating at a central frequency of 17.2 GHz with a chirp bandwidth of 200 MHz. This ground-based radar is an extension of the gamma portable interferometer (GPRI), designed and built by GAMMA Remote Sensing [31], [36], with fully polarimetric capabilities [37] and the possibility of operating, in addition to the monostatic configuration [Fig. 4(a)], in bistatic mode [Fig. 4(b)] [38].

KAPRI shares the same characteristics as its single-polarimetric counterpart: a nominal range resolution of 0.75 m and an azimuthal resolution of 7.5 m at a 1-km LOS distance [39]. According to the specifications provided in [40], for differential interferometry of the monostatic, the deformation measurement precision is 0.03 mm with an SNR of 30 dB and 0.125 mm when the SNR is 20 dB. The accuracy of the deformation is less than 1 mm at 1-km distance subject to variations on the atmosphere, mainly, disturbances caused by atmospheric water vapor.

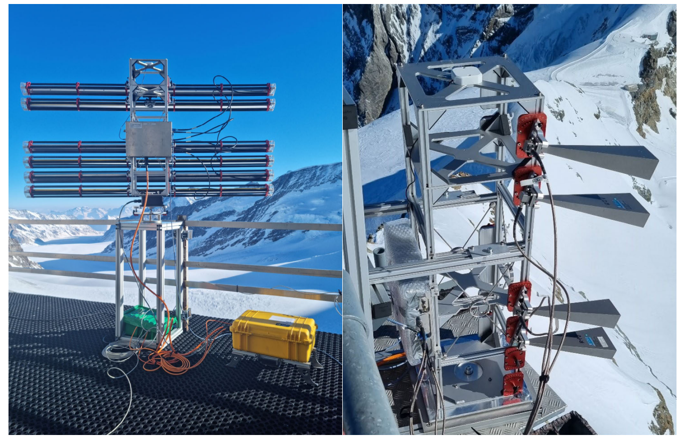

(a) (b)

Fig. 4. KAPRI configurations. (a) KAPRI monostatic device (primary device). (b) KAPRI passive receiver in Ostgrat terrace (secondary device).

Instead of the three antenna configuration, KAPRI uses a six-narrow-beam antenna configuration, two transmitters, and two pairs of receivers in horizontal and vertical polarizations that rotate over an axis. The bistatic or secondary receiver, as the name indicates, is characterized by four receiving-only wide-beam horn antennas, one pair for each polarization, devoid of any motion. Despite the wide-beam nature of the antennas, the nonrotating secondary receiver results in a narrower illumination of the scene than in monostatic acquisitions, degrading image quality on the sidelobes (see Section III-A). In this study, however, only the vertical polarization dataset has been used, de facto returning to the single-polarization mode of the instrument, because the experimental focus was on the bistatic configuration.

The particular instrument's positioning was as described in [41, Table I], in which the primary device is deployed at the High Altitude Research Station of Jungfraujoch and the secondary was approximately located 1 km away, about 200 m higher on an exterior terrace of *Ostgrat*, achieving a bistatic baseline of ≈ 960 m [29]. The geometry of this configuration leads to strong variations of the bistatic and look angles. The bistatic angle, close to 90° in the near range and tending toward 0° in the far range, and the look angle approximately 50° in the near range and above 90° in far-range mountain tops above the radar.

A. Loss of SNR in Bistatic Configuration

As mentioned in Section III, the bistatic receiver detects signals that form a bistatic angle β with the transmitted ones. If the target mostly presents backscattering and has moderate or low scattering in the other directions, this results in lower bistatic SNR than monostatic ones. In addition, the nature of the acquisition itself also contributes to a lower bistatic SNR: the primary device transmits (and simultaneously receives) a narrow beam signal, which illuminates a narrow section of the scene following an azimuth rotation. While the primary device antennas are always pointing to the target area, the

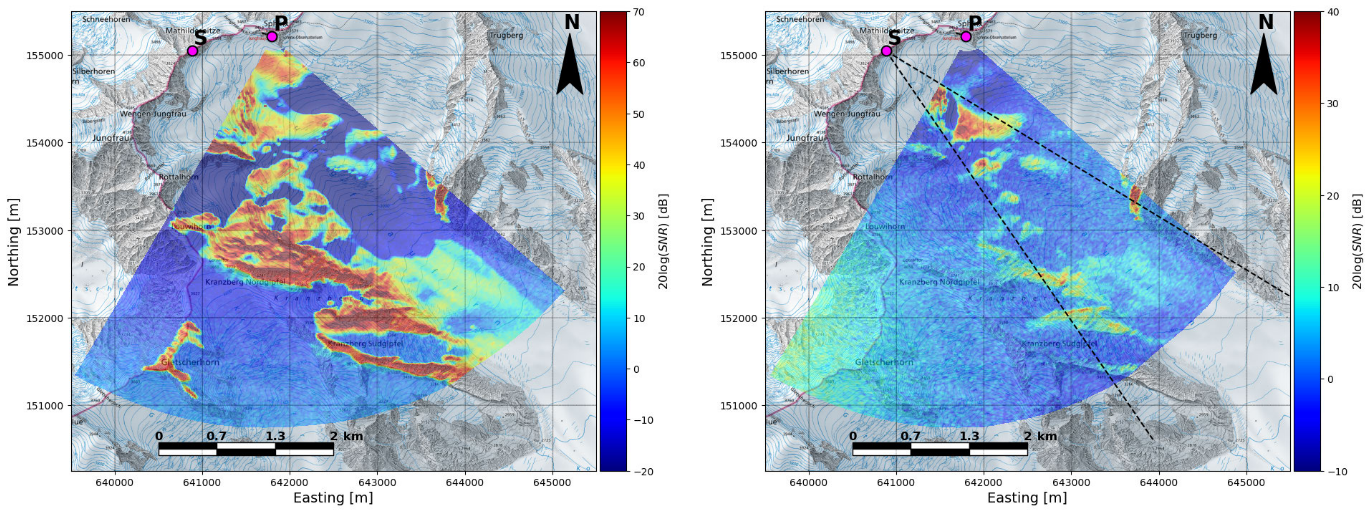

(a) (b)

Fig. 5. Map of the SNR across the scene expressed in decibels (dB). (a) Monostatic SNR. The SNR reaches its maximum values in the regions where all the signals are reflected, namely the rock facies in the mountains. Its value decays as the range increases due to the loss of the returning signal power and the incident electromagnetic wave becoming tangential to the surface. (b) Bistatic SNR with linear trend of noise model. Dashed lines indicate the reception beamwidth of the secondary device. Similar to the monostatic case, high SNR regions are found in the near-mid range. Due to the different direction of the reception leg compared to the transmitting leg and the use of static wide-beam antennas, the SNR is considerably lower in the whole scene.

secondary device's wide-beam antennas remain static pointing to the same region, leading to an SNR loss toward the edges of the viewed scene, becoming more noticeable as the range increases. Fig. 5 shows the SNR of the scene according to monostatic and bistatic acquisitions. One can notice in Fig. 5(b) that, as expected, the highest SNR is at the center of the reception beam (dashed line) and in the near range. The SNR is of great importance as it has a direct impact on the coherence of the interferograms, being a source of decorrelation. Therefore, a loss of SNR will translate into a loss of coherence and eventually lead to less data points that are above the coherence threshold described in Section II. As a result, bistatic acquisitions suffer from a reduced image quality compared to monostatic ones.

IV. Campaign and Dataset

The selected dataset corresponds to the March 2, 2022 acquisitions [29] and consists of a time series spanning from 09:01:30 h to 10:13:30 h (both UTC time), with a sampling interval of 1.5 min. The chosen time period corresponds to a set of consecutive raw differential interferograms, particularly stable after being visually inspected to detect phase anomalies caused by wind or clouds. To the best of our knowledge, these acquisitions constitute the first bistatic differential interferometric dataset on a glacier where targets are at a kilometer-scale distance.

The extent of the radar images comprises a near-range area of approximately 200-m distance from the primary device and up to a 4-km distance toward Konkordia Platz. Fig. 6(b) shows the observable region from the point of view of the primary device. As it can be seen, the area is rather narrow, surrounded by mountain peaks that reach 4000 m and the glacier surface is characterized by multiple slopes that block the radar illumination and result in shadowed regions, as seen in Fig. 6(a). Regions of interest (ROIs) of the radar images have been delimited to study the glacier displacements locally. The regions are described as follows: ROI 1 is located on the near region of the radar approximately 200 m away from the primary device and 800 m from the secondary device. The region of moderate slope toward the southeast follows the glacier flow. ROI 2 is located on a steep slope that combines exposed rock with snow-covered areas as well as ice. Some of these areas are perpendicular to the radar signal. This explains the high backscatter intensity displayed in Fig. 6(a). The distance from the primary and secondary is about 3 km. ROI 3 is a far-range region leading to Konkordia Platz, at a distance from the radars of about 3.5–4 km. It is characterized by a rather flat area with a gentle slope to the southeast. Finally, ROIs 4 and 5 are regions shadowed by the terrain topography that are used as noise reference for later calculations. These ROIs are located behind the nearby mountains on the right that appear in the photograph [Fig. 6(b)]. ROI 6 is also a base-noise region only considered for the bistatic SNR calculations. Complementary to the dataset, an external DEM (SwissALTI3D©) is necessary to perform the geocoding and as a source of the topography-derived parameters. This choice is made for two reasons: first, in order to calculate the precision loss across the whole study region without data gaps caused by low coherence, and second, to ensure a homogeneous resolution cell across the scene (4×4 m). KAPRI-derived DEM suffers from these two aforementioned problems and still requires the external DEM to perform interferometric phase unwrapping. In Section VI-A, the consequences of our DEM choice are addressed.

V. Analysis of the Results

In this section, we present the displacements derived from the monostatic and bistatic differential interferometric phase

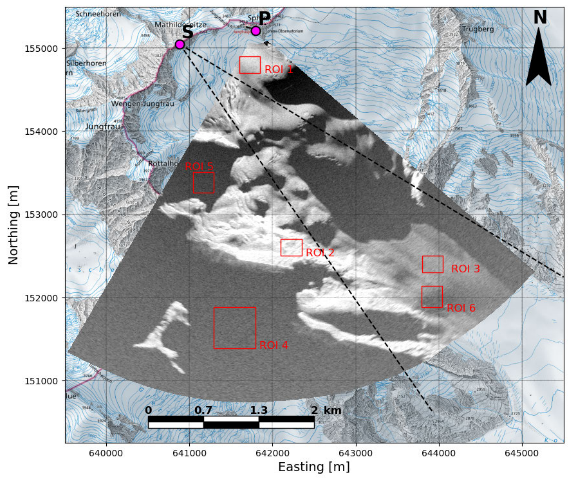

(a)

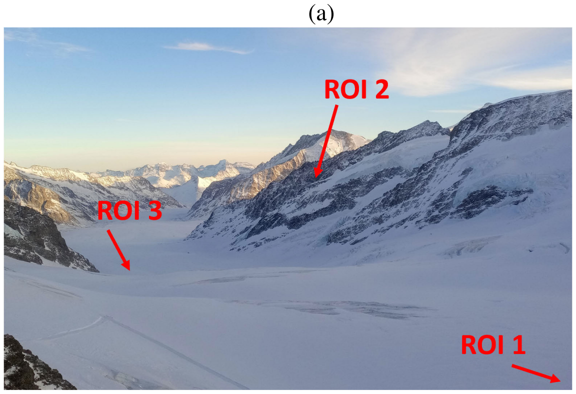

(b)

Fig. 6. Location of the observation area and ROIs. (a) Map of the fieldwork area on Jungfraufirn region, Great Aletsch Glacier. Location of the radar primary (P) and secondary (S) radar devices is labeled accordingly. The observable region by the radar devices is shown by the monostatic multilook image on grayscale on top of map underlay of the Landeskarte 1:25 000, ©Federal Office of Topography (Swisstopo). (b) Image of the fieldwork area taken from an exterior terrace at the High Altitude Research Station of Jungfraujoch (primary device location). The locations in the picture of the different ROIs are pointed out with an arrow. ROI 1 is outside the picture toward the direction indicated.

datasets. The magnitude and three independent directions (east, north, and vertical to the local plane) of the displacement vector are calculated according to the monostatic formulation (Section II-A) and the monostatic–bistatic formulation (Section II-B).

A. Magnitude and Direction of the Displacements

The magnitude and direction of the displacement vector are presented in Fig. 7. Fig. 7(a) and (b) shows the eastward and northward components of the displacement forming a 2-D vector map for the monostatic and the monostatic–bistatic approaches, respectively. Fig. 7(a) depicts both in magnitude and direction the first two components of the vector defined in (6). It is characterized by a smooth vector field with the exception of few discontinuities on steep-slope areas and outliers in the far-range areas of the scene. In contrast, the magnitude of the displacement is heterogeneous across the scene regardless of the SNR. Fig. 7(b) shows the results for the monostatic–bistatic case, in which the first two components of the vector obtained in (15). The displacement vector using the monostatic–bistatic formulation presents smoothness both in magnitude and the vector field. There is a clear difference between the results in the near range and the far range, the latter, presenting a higher spatial variability in the magnitude as well as on the calculated glacier flow bearing direction. This is to be expected as the signal arriving to the passive receiver from the far range is barely above the noise level, as shown in Fig. 5. Overall, the direction of the displacements using the monostatic–bistatic approach is in accordance, especially in the near range, with the monostatic-only approach, meaning that the assumption of a glacier flow moving in the direction of the maximum gradient of the topography is reasonable. Regardless of the method applied, the stability of the vector direction degrades in the far range, correlating with the loss of signal and worsening azimuth resolution.

Fig. 7(c) and (d) illustrates the vertical component, which is perpendicular to the northeast plane corresponding to the monostatic and monostatic–bistatic derived vertical displacement, respectively. In particular, in the monostatic case, the vertical displacement component corresponds to the vertical component of the parametrised surface gradient vector $\hat{g}_z$ [see (6)]. In the monostatic–bistatic case, the vertical component is s_z of the displacement vector obtained when solving the system in (15). In both cases, there is a clear division between two regions: the glacier area, rather flat, and the steep slopes toward the southwest of the scene. The glacier region presents mostly vertical null displacements or approximately an order of magnitude lower than the easting–northing component. The steep-slope areas present either negative (downward) and positive (upward) vertical components, the latter associated with a mathematical artifact when calculating the gradient (discussed in Section VI-A). These results indicate that not only is it possible to use the DEM gradient as an approximation to the glacier flow, but it also confirms that the areas on the glacier tongue can be modeled by a simpler 2-D flow.

Fig. 8 shows the stereographic plots with the directions and histograms of the magnitudes of the displacement vector corresponding to three different ROIs. On the left, the stereographic plots represent the full 3-D vector by means of a wind rose depicting the bearing (angle corresponding to the easting–northing direction) and a concentric grid for the elevation (vertical direction angle). The right-hand side of Fig. 8 shows a histogram of the magnitude values of the displacement vector derived using the monostatic and the monostatic–bistatic approaches. Table I complements the information by providing numerical values describing the main statistical parameters of the displacement distributions.

Following an ROI-by-ROI analysis, ROI 1 [Fig. 8(a) and (b)] presents hardly any discrepancy between the results obtained by either applying the monostatic approach or the monostatic–bistatic one. As previously stated, it is clear that the near range is favorable for both cases in terms of having a higher SNR as well as approximately a squared resolution cell. In accordance with the characteristics of the scene, the direction of the displacements follows a gentle downward slope with a negative elevation angle, close

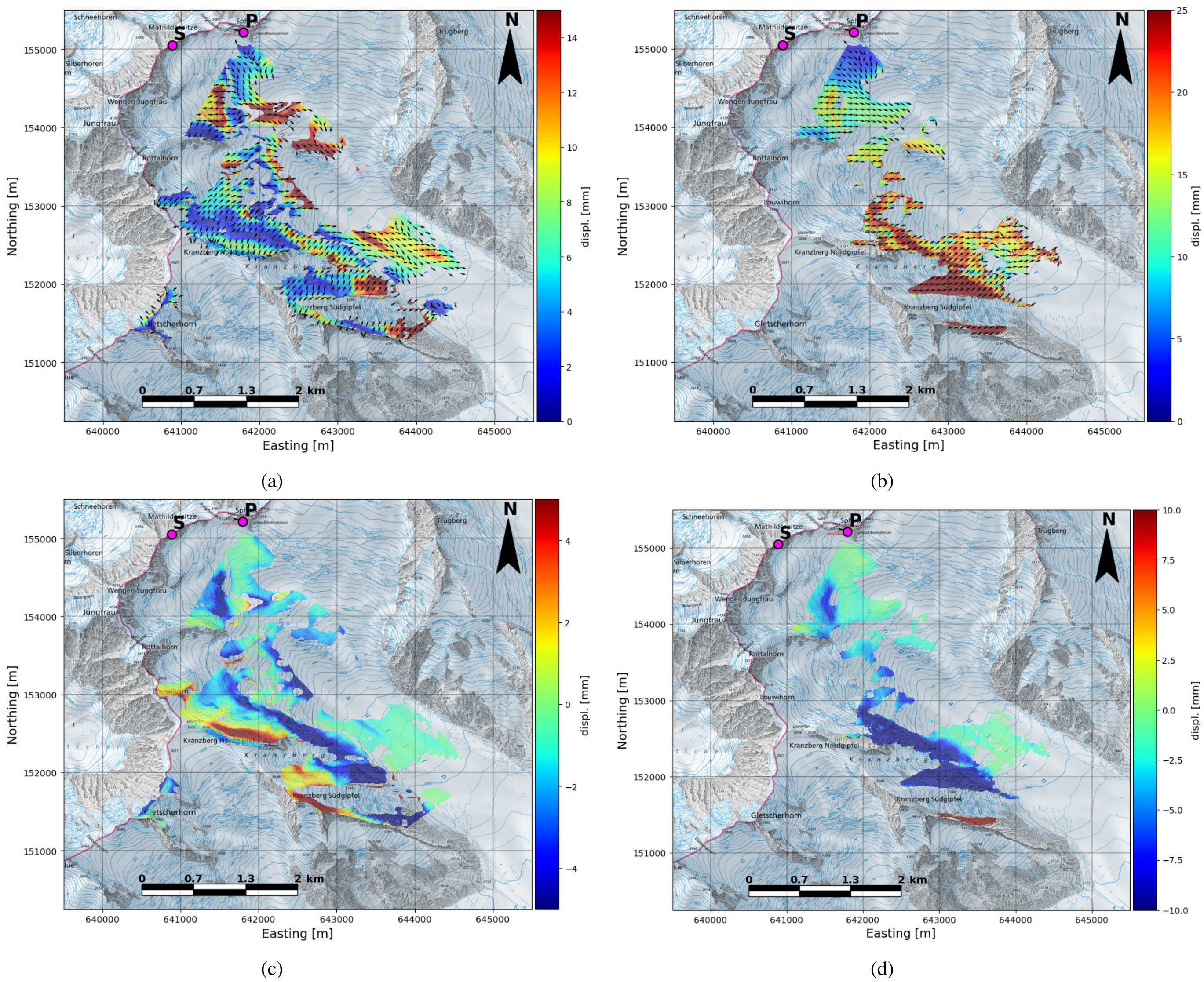

Fig. 7. Comparison of the monostatic and monostatic–bistatic calculated displacements. Magnitude of the displacements in *mm* as a heatmap and a normalized 2-D vector field with direction projected over the eastnorth plane, corresponding to the first two components of the 3-D displacement vector $\vec{s}$ (a) monostatic derived displacements and (b) monostatic–bistatic derived displacements. Vertical component of the displacements (c) vertical component using the monostatic dataset and (d) monostatic–bistatic derived vertical displacements.

TABLE I

MEAN, MEDIAN, AND STANDARD DEVIATION VALUES FOR THE MAGNITUDE AND DIRECTION ANGLES OF THE DISPLACEMENTS FOR THE FIRST THREE ROIS. THE VALUES PRESENT THE ACCUMULATED DISPLACEMENT FOR THE 09:01:30 H TO 10:13:30 H. THE ANGLES ϕ AND θ CORRESPOND TO ELEVATION AND BEARING, RESPECTIVELY

	ROI 1		**ROI 2**		**ROI 3**	
	Monostatic	Bistatic	Monostatic	Bistatic	Monostatic	Bistatic
mean $\lvert\vec{s}\rvert$ **[mm]**	3.83	4.42	2.63	19.23	8.54	17.82
median $\lvert\vec{s}\rvert$ **[mm]**	3.84	4.56	1.96	18.03	8.41	17.32
std. dev. $\lvert\vec{s}\rvert$ **[mm]**	1.17	0.85	2.41	8.44	1.04	4.80
mean ϕ [°]	-6.42	-6.15	-17.21	-42.59	-3.27	-2.31
median ϕ [°]	-6.07	-5.96	-46.31	-43.56	-3.16	-2.48
std. dev. ϕ [°]	1.68	1.58	45.04	7.82	0.42	1.00
mean θ [°]	139.11	132.21	-11.51	72.76	122.81	80.04
median θ [°]	138.48	129.29	44.46	75.47	120.18	78.24
std. dev. θ [°]	17.10	17.25	86.03	18.13	21.03	12.56

to 0°. This is true for the magnitude, in which the monostatic–bistatic approach performs slightly better, presenting fewer outliers than the monostatic ones. These results are supported by the values in Table I.

ROI 2 [Fig. 8(c) and (d)] presents a high discrepancy in the direction of the displacements, not in bearing, but in elevation. The monostatic results for the elevation show two clusters: one with a negative direction (indicating downward motion) with

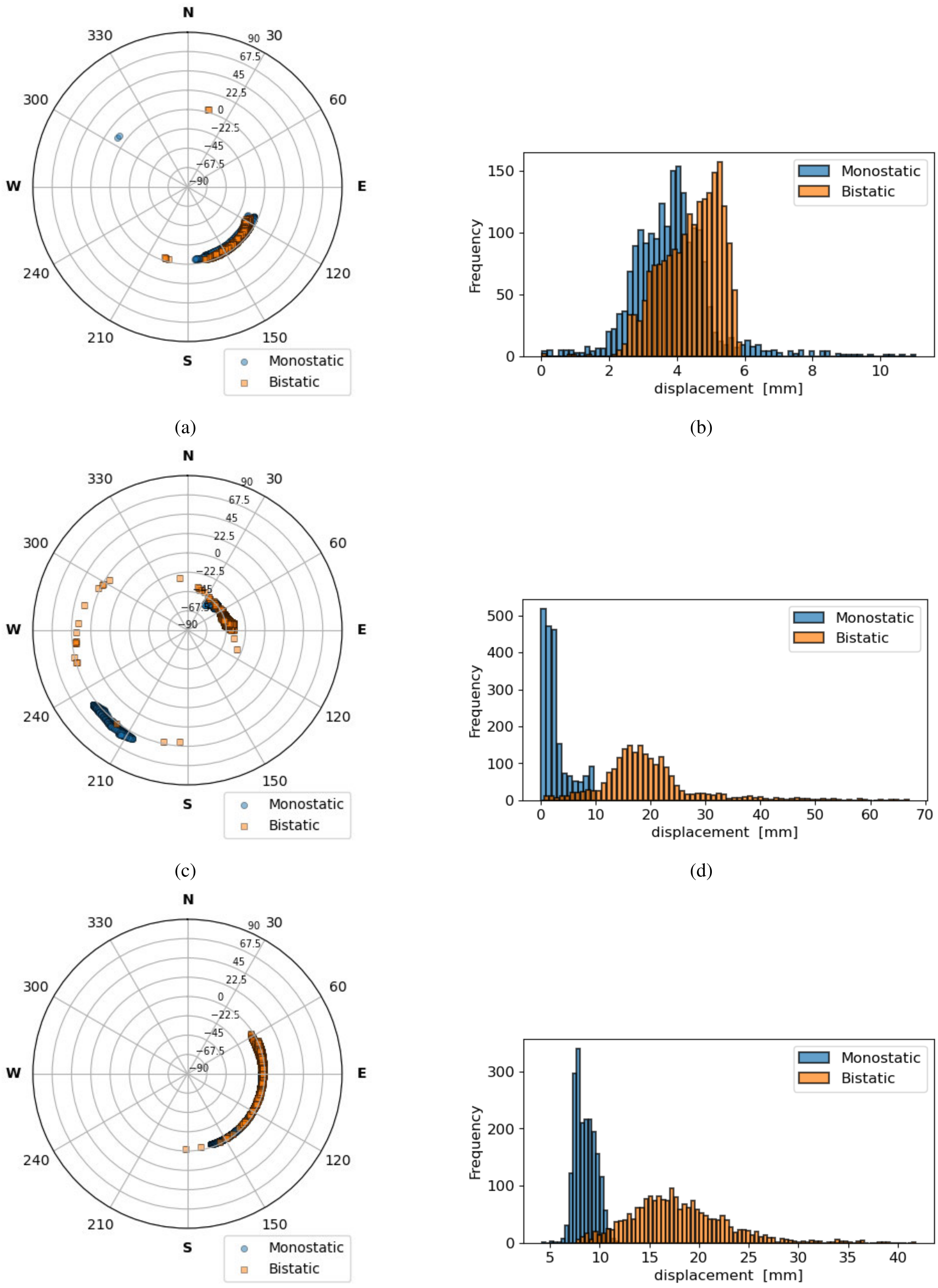

(e) . (f)

Fig. 8. Comparison between monostatic and bistatic displacement direction and magnitude at different ROIs—ROI 1: near-range glacier, ROI 2: mid-range steep regions, and ROI 3: far-range glacier. (a) ROI 1, (c) ROI 2, and (e) ROI 3 [stereographic plots show the bearing direction (cardinal points) and the elevation (grid lines)]. (b) ROI 1, (d) ROI 2, and (f) ROI 3, showing the histogram of the point-wise difference between the monostatic and the bistatic displacement magnitudes. While both datasets present similar directions and magnitude values of the estimated displacements in the near-range region (ROI 1), the increment of range has a direct and unequal impact on the standard deviation of the datasets. This can be observed in the histogram for ROI 3 in which the bistatic dataset has significantly spread over a larger range of values compared to the monostatic results in (a).

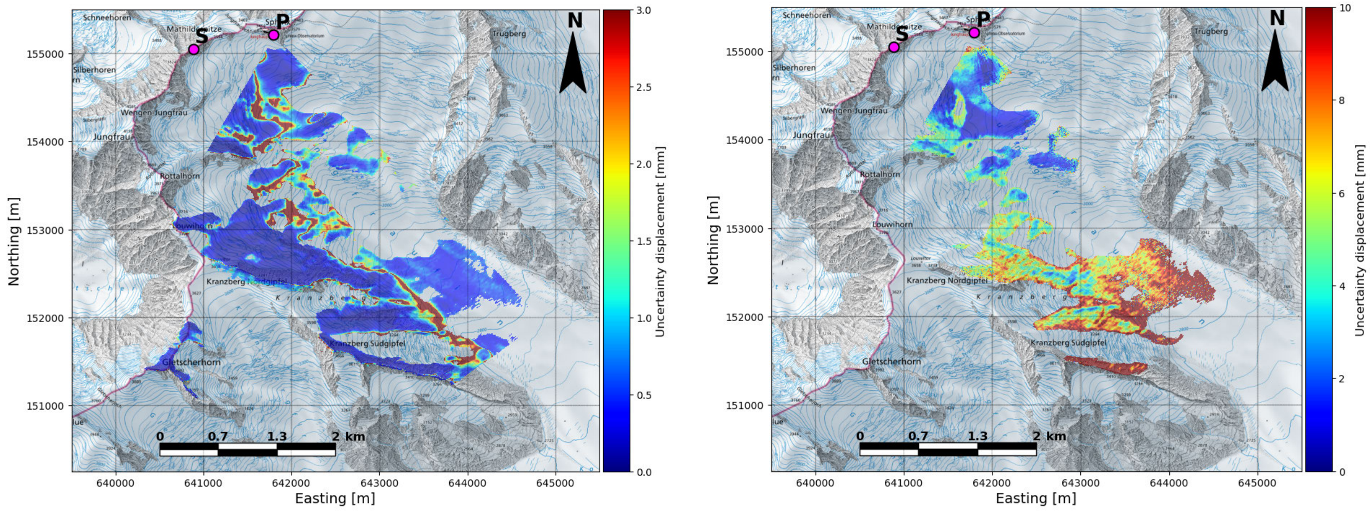

(a) (b)

Fig. 9. Displacement uncertainty. (a) Monostatic case. The uncertainty value is within the submillimeter level across the whole scene thanks to the high SNR [see Fig. 5(a)]. The areas in which the uncertainty is exceptionally high is because the the value of $\gamma \approx 90°$, and despite a high SNR, the value of $\sigma_{||s||}$ [see (13)] tends to infinity. (b) Monostatic–bistatic case: the uncertainty has submillimeter values in the near and mid range, while it reaches above-millimeter level values in the far range. The main driver for these variations is the fast decay of SNR in the scene as seen in Fig. 5(b).

a value of $\approx -45°$ and another cluster with positive values (meaning upward motion) with a value of $\approx 45°$. The latter, in principle, display a counterintuitive behavior: they present a positive s_z value, which would imply that the glacier is moving up the mountain slope. If one observes the histogram of Fig. 8(d), most of these displacements are actually an almost-zero displacement in the monostatic dataset. This is to be expected considering that the signal coming from ROI 2 is from a nearly perpendicular area to the radar positioning [Fig. 6(b)], hence, invisible in the LOS of the monostatic device. The combination of the extreme local gradients with LOS displacements close to zero means that a slight change in the sign of the displacement induces the opposite direction (upward versus downward) in reconstruction of the displacement (further discussed in Section V-B). In this case, while the monostatic–bistatic shows an increased standard deviation on its magnitude values, the consistency in bearing and elevation clearly outperforms the results obtained by the monostatic-only (Table I).

ROI 3 [Fig. 8(e) and (f)] targets an area in the far range of the glacier tongue toward Konkordia Platz. In this region, the directions obtained by using the monostatic and the monostatic–bistatic formulations are on a par and have similar mean and standard deviation values (Table I), describing a quasi 2-D motion. The monostatic–bistatic magnitude histogram becomes flattened, also with growing outliers. This behavior is expected as the deterioration of the SNR in the bistatic receiver is significantly different from that of the monostatic acquisition, having a direct impact on the reconstruction of the displacements. According to [29, Table 3.4], the slant-range drift from Aletsch glacier in Jungfraufirn region is estimated to be between 21 and 23 cm per 24 h. This translates roughly about 9 mm/h toward the far-range area, corresponding to the one obtained 8.55 mm using the monostatic method (Table I, ROI 3).

The main findings can be summarized as follows.

1) Monostatic-derived magnitude of the displacements can be assumed to have a standard deviation independent of the range. In contrast, monostatic–bistatic magnitude shows an increasing standard deviation with increasing range.
2) The monostatic–bistatic approach is more robust for the calculation of the direction of the displacements. This is shown by consistently low standard deviations in elevation and bearing angles with independence of the range distance. Results worsen in ROI 2 (mid-range), but this is attributed to the challenging topography.
3) Taking into account the previous statements, the two approaches present higher similarities in the near range (ROI 1), both ranging in magnitude approximately about 4 mm (mean value) and a standard deviation of $\approx$ 1 mm.

B. Uncertainty of the Displacements

In order to evaluate the validity of the displacements, we explore the error propagation (Fig. 9) and the digit precision loss [Fig. 10(b)]. The error propagation allows a direct comparison between the uncertainties in the monostatic and bistatic methods as both rely on the SNR of the scene [see (14)]. As expected from the SNR values, in general, monostatic data are characterized by a high SNR across the scene, driving uncertainty lower than the bistatic counterpart. Therefore, high uncertainty regions in the monostatic case for our scene are not originating from a low SNR but from its geometry. As shown in (25), the monostatic-derived displacements present a discontinuity when γ is 0°. This occurs when these two vectors are perpendicular; in other words, when the angle between these two vectors, γ, is 90°. Interestingly, the geometry in steep-slope regions, such as ROI 2, is also expected to have γ angles well above 60° and consequently higher uncertainties, but data show otherwise. A possible

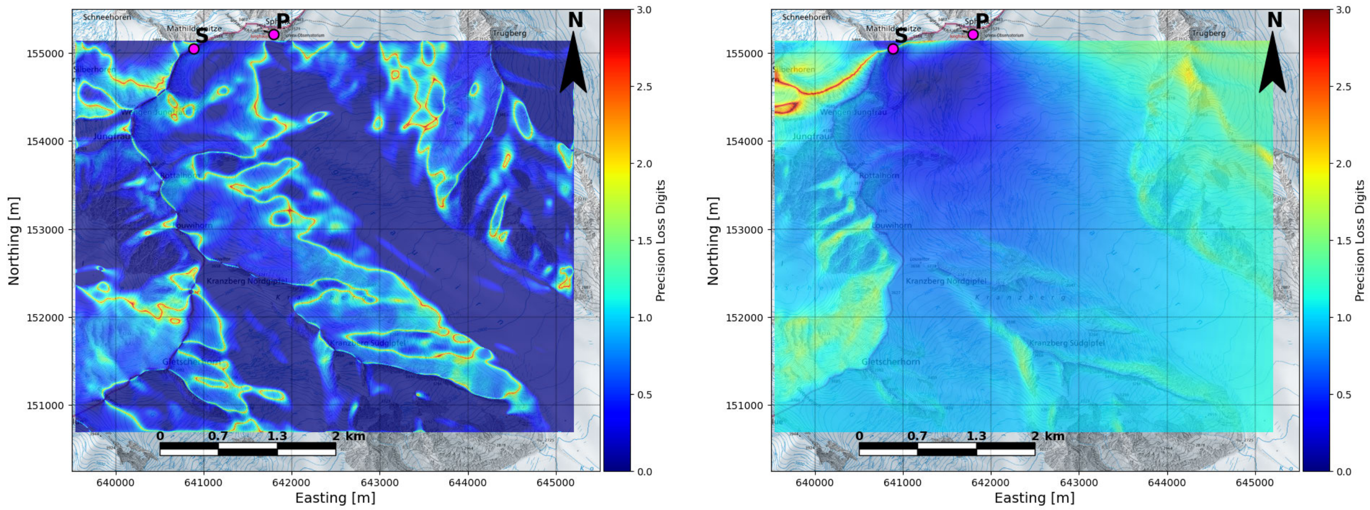

(a) (b)

Fig. 10. Digit precision loss. (a) Monostatic case: only the relative position of the primary device (P) with respect to the target and the local topography influences the condition number. Regions in which $\vec{u}_m$ is perpendicular to $\hat{g}$, such as steep mountain regions, result in several digits of precision loss. (b) Monostatic–bistatic case: note that the respective positions of the primary (P) and secondary (S) devices in combination with the scene topography are the drivers for the values of the digit precision loss. For this reason, the regions in which the angle between $\vec{u}_m$ and $\vec{u}_b$ is 90° or that $\vec{n}_t$ is parallel to the normal of the LOS plane, the digit precision loss is low.

TABLE II
STATISTICAL SUMMARY OF THE DISPLACEMENT UNCERTAINTY, ROI-WISE

		ROI 1	**ROI 2**	**ROI 3**
Monostatic	**mean**	0.45	0.19	0.39
Uncertainty	**median**	0.22	0.17	0.38
[mm]	**std. dev.**	4.73	0.09	0.06
Monostatic-Bistatic	**mean**	3.37	6.35	8.77
Uncertainty	**median**	3.33	6.39	8.79
[mm]	**std. dev.**	1.14	1.30	1.48

interpretation is that the exceptionally high SNR brings the monostatic phase uncertainty value to 0 [see (14)], virtually canceling the geometric contributing term dependent on γ.

Results in Fig. 9 are complemented by a statistical overview of the uncertainty values on an ROI-by-ROI basis, in Table II. The localized analysis of the uncertainty allows to get a deeper look into some implications already hinted at when observing the entirety of the scene. In the monostatic case, the uncertainties are submillimeter level, and they can be expected to hold to the presented values robustly within the studied regions. However, this is not the case for ROI 1. The reason for this is that ROI 1 contains regions where the γ value is close to 90°, leading to high uncertainties [see red regions in Fig. 9(a)]. While these values are geographically localized and increase the standard deviation of the whole ROI, they cannot be discarded as outliers. They do represent a high uncertainty triggered by a specific feature in the terrain that highly impacts the reconstruction of the displacement. In the monostatic–bistatic case, as expected, uncertainty values are higher, on the millimeter level. The uncertainty distribution shows a proportional increase of uncertainty with increasing range: in the near range (ROI 1) is about 3 mm; by the mid range (ROI 2), it is slightly above 6 mm; and in the far range, it has almost trippled, approaching 9 mm. The standard deviation remains almost steady, indicating the smoothness within the ROIs.

Fig. 10 shows the digit precision loss when reconstructing the displacements in the monostatic and monostatic–bistatic cases. For both, this uncertainty value results from the calculation of the condition number [see (32)] and reflects exclusively the influence of the geometrical configuration on the error. For this reason, as the SNR is not accounted for, nor are other differential interferometric data-derived parameters (such as coherence), the extent of the map corresponds to the full extent of the external DEM. If comparing these results with those obtained in Fig. 9 and Table II, one can see how much SNR influences their uncertainties. In the monostatic reconstruction of displacements, it is confirmed that the SNR is so high across the whole scene that uncertainty is below the submillimeter level except for areas with extreme features. When looking into the digit precision loss caused by the geometry [Fig. 10(a)], it is clear that many regions are unfavorable to reconstruct displacements, namely, steep-slope areas. For the monostatic–bistatic reconstruction of displacements, the SNR plays an opposite role. The geometrical configuration is highly favorable across the scene, and it is in fact its low value the main source of uncertainty. The geometrical-only approach shown in Section II-D clearly underestimates the uncertainty, particularly in the far range.

VI. DISCUSSION

A. Comparison Between Monostatic and the Bistatic-Derived Displacements

The displacement heatmap and vector map of Fig. 7(a) shows a lack of homogeneity in the displacement field. Both the magnitude and the direction present evident discontinuities that on a first assessment do not seem to correspond with the actual behavior of the glacier flow. These inconsistencies are also evident when observing the vertical component in Fig. 7(c). One would expect that for the slope areas where the estimated flow is pointing only downhill, the displacement would be evident; instead, the map presents several direction variations between negative (downhill), zero, and positive (uphill) values. These results are not linked to the physical behavior of the glacier flow on steep-slope areas but are an artifact of the method. It must be recalled that the monostatic-derived displacement magnitude is completely uncoupled from its direction. As elaborated in Section II, the direction of the displacement vector is imposed by the gradient of the DEM, which constitutes an independent dataset from the one retrieved with the radar. This provokes some differences. First, the DEM does not match the time of the observation (actually, the DEM is updated every six years), resulting in either extra or missing features in comparison to the radar dataset. Additionally, the DEM has a constant resolution grid in which some complex terrain features such as crevasses and rock formations are captured. In contrast, the radar images are real-aperture, meaning that the resolution cell increases with range and the sensitivity to such detailed features decreases. Even after smoothing the DEM with a Gaussian filter, some of these features remain and have a distorting effect upon the direction of the displacement as they do not truly point to the hypothetical glacier flow direction. Second, the technique for the DEM generation is LiDAR, implying that the values of the DEM are strictly at the surface level. This is not necessarily the case for KAPRI's data. In fact, the high-frequency signal has depth penetration depending on the snow conditions of temperature, water content, snow density, and so on, and as a general rule, the phase center does not correspond to that of the glacier surface. Finally, there are regions in which a small change in the magnitude of the displacements can trigger a 180° change in the direction of the displacements, resulting in a heterogeneous displacement field. This effect is notorious in mountain steep regions where γ is close to 90° [as shown in Fig. 10(a)], meaning that the uncertainty of the displacement is high. In such a case, a change of sign in the LOS displacement translates into a vector direction that points upward instead of downward [Fig. 7(a)].

The bistatic-derived displacements [Fig. 7(b) and (d)] present some particularities compared to the monostatic ones. A notable difference is that the displacements are more homogeneous, showing a smooth transition (both in magnitude and direction) between regions. In fact, the displacements start to become erratic on the far range, and as formerly stated, this is attributed to a severe decay of the SNR. The vertical displacements, shown in Fig. 7(d), present more reasonable values. The glacier tongue region is expected to move in a 2-D fashion: the vertical displacements of this region corroborate this, showing values close to zero. The mountain steep region is characterized by negative s_z values, indicating the gravity-induced downward motion of the glacier. Only one mountain top in the far range presents positive vertical values. However, this same region is shown to have high uncertainty values [see Fig. 9(b)] associated with a very low SNR on the bistatic receiver, and therefore, they are not reliable. It needs to be highlighted that in the bistatic method, both magnitude and direction of the displacements are determined by the combination of the differential interferometric phase on the primary and secondary devices. In this case, the external DEM is used to restrict the plane in which the displacement is contained, but not the actual direction. Thus, it reduces potential mismatches between features included in the DEM but not on the radar data and vice versa. However, a major drawback is that when phase differences are close to zero value, noise effects take over and they affect both the magnitude (which would correspond to the zero displacement) and the direction. This is evident in the near-range region of Fig. 7, characterized by near-zero displacement magnitudes, in which some vectors seem to have arbitrary directions.

In general terms, the direction of the monostatic and bistatic-derived displacements is almost identical in the near range and on the overlapping mountain regions. The two bearings start diverging as the range increases, to which it is attributed to the lower SNR of the bistatic data. This means that assuming the direction of the displacement as the one of the gradient of the topography is a good approximation. On the other hand, the magnitude values as well as its distribution differ considerably. To assess which of the approaches might be closer to the actual values, an ROI-by-ROI analysis is needed.

1) Analysis of the Displacements ROI-Wise: The ROI-by-ROI comparison shown in Fig. 8 presents for each ROI a stereographic plot depicting the direction of the displacement (bearing and elevation angles) as well as a histogram of the displacement magnitudes. On the one hand, it can be appreciated from Fig. 8(a), (c), and (e) the robustness of the bistatic method to calculate displacement directions. Also, it can be contrasted with the numerical data of Table I showing lower standard deviations on bearing and elevation than the monostatic counterparts. On the other hand, the magnitude presents the opposite behavior: the bistatic-derived displacements present, in general, a higher standard deviation that manifests as rather spread out distributions on the histogram [also, supported by the uncertainty of the magnitude of the displacements shown in Fig. 9(a) and (b)]. Near-range ROI 1 is the one presenting the highest similarity between monostatic and bistatic results, both in direction and magnitude. This result is as expected, given that the near range presents a higher SNR in both monostatic [Fig. 5(a)] and bistatic [Fig. 5(b)] acquisitions, higher resolution, and for the bistatic, an optimal geometrical configuration to minimize errors ($\sin\beta$ close to 1). For the case of ROI 2, the situation changes: the region is already considered mid-to-far range, and given the extreme slopes of the terrain, both methods struggle to deliver good results. The histogram in Fig. 8(d) shows that while the bistatic method predicts displacements on the order of 20 mm, the monostatic is one order of magnitude lower. While the bistatic results rather overestimate the actual displacements, the monostatic cannot either be taken as a reference. Steep slopes constitute unsuitable viewing geometries when reconstructing the topography using an airborne-derived DEM [36]. This is reflected in anomalies on the monostatic magnitudes distribution shown in Fig. 8(d) (differing from a normal distribution) and two clusters in Fig. 8(c) with opposing bearings leading to extreme

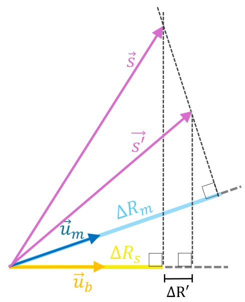

Fig. 11. Influence of low bistatic SNR on displacements vector. This 2-D simplified diagram illustrates how a relatively small noise-induced LOS displacement $\Delta R'$ changes the displacement direction significantly, from $\vec{s}$ to $\vec{s}\,'$, while the magnitude remains similar.

standard deviation values. Results in Table I also express high variation in addition to the nonsymmetry of the dataset, characterized by a left skewness. For the case of ROI 3, bistatic-derived magnitudes are twice those of the monostatic-derived. According to in situ measurements, the monostatic method is the most accurate. The reasons for the unsuitability of the bistatic method on the far range are twofold: loss of signal [low SNR, see Fig. 5(b)] and LOS vectors tending to colinearity. As mentioned before, in the bistatic method, a change in the differential interferometric phase impacts not only the estimated magnitude but also the direction. This is key to comprehending the resulting directions dominated by the secondary LOS vector. The noise in the far-range region is high enough to produce a nonzero noise-induced LOS displacement component ($\Delta R'$) that generates a distorted displacement $\vec{s}\,'$ in magnitude and direction, just as shown in Fig. 11.

B. Limitations of the Monostatic and the Bistatic Methods for Displacement Derivation

Each approach has different strengths and weaknesses, which deserve further attention as they are not fully captured by the uncertainty propagation or digit precision loss plots. First, one must differentiate between limitations stemming from low SNR (captured by the uncertainty of the displacements, see Fig. 9) and by purely geometrical constraints (Fig. 10).

It is clear that for the case of monostatic displacements, SNR does not constitute a limitation (in this study), as shown in Fig. 5(a), however, the geometry is. The monostatic approach relies on the use of a single radar device, meaning that the only available information is in the primary's LOS direction. Hence, to obtain the displacements in the three directions of space, the gradient of the DEM topography is imposed. Consequently, this choice results in geometrically unsolvable points that lead to high uncertainty and high precision loss regions as seen in (13) and Fig. 10(a). Indeed, the red areas correspond to the geometric locus in which the monostatic LOS and the topographic gradient are perpendicular, causing a sharp increase of the condition number [see (27)]. An additional factor that eludes uncertainty and precision loss plots comes from the decoupling of the magnitude and direction of displacements in the monostatic formulation. Using a LiDAR-derived DEM for the directions results in discontinuities in the displacement map that are not explained by physical causes but rather by a mismatch of the two datasets. The DEM describes the topography strictly at surface level, while radar images are expected to have some penetration or they include detailed surface features (e.g., crevasses or rocks) that might no longer be present in the actual scene. Furthermore, the LiDAR-derived DEM's own error propagation is not considered, even though it is known that, contrary to the radar acquisitions, high uncertainty of the terrain reconstruction occurs in the steep mountain regions (see Section VI-A1).

The monostatic–bistatic approach is able to reconstruct the direction of the displacements more robustly; therefore, its main limitations come from the low SNR rather than from the geometry of the scene. This seems clear when observing Fig. 9(b) and one compares it to the bistatic SNR [Fig. 5(b)] and precision loss [Fig. 10(b)]. The SNR decay is the main cause of the uncertainty increase in the far range. Precision losses associated with moving away from the geometric locus where the secondary and primary LOS vectors intersect at $\beta = 90°$ [see (18)] or due to being collinear to n_3 (nearby peaks and mountainous chains) fall into a category of second-order effects. Nevertheless, these two factors do not account for the consequences of coupling the magnitude and direction of displacements. The major drawback is that the final direction of the displacement is susceptible to artifacts affecting the magnitude, such as atmospheric disturbances. Being particularly critical if their order of magnitude approaches that of the magnitude of the displacement itself, just as shown in Fig. 11. In other words, even for a target area under favorable geometry ($\beta = 90°$) and with high SNR, relatively small perturbations in magnitude caused by the atmosphere can trigger large changes in direction of the displacement vector.

C. Impact of the Bistatic Angle on Error Propagation and Precision Loss

In this study, the suitability of the bistatic configuration has been analyzed by calculating the precision loss over the scene. However, these results are bound to the specific geometry of the observing site. In order to make a broader assessment under which conditions the usage of a bistatic configuration might be geometrically favorable, it is necessary to explore the variation of the condition number κ with the bistatic angle β and other geometrical parameters that restrict the problem.

Take the most simple of scenarios in which the topography is completely flat, effectively restricting the problem to 2-D. In that particular scenario, the set of equations defined in (18) would be reduced to

$$\begin{cases} s_1 = \dfrac{\lambda}{4\pi}\phi_m \\ s_1 \cdot \cos(\beta) + s_2 \cdot \sin(\beta) = \dfrac{\lambda}{2\pi}\phi_s \\ s_3 \cdot n_3 = 0. \end{cases} \tag{33}$$

Given that in a purely 2-D case, both LOS vectors would be contained in the XY plane of the topography, it is understood

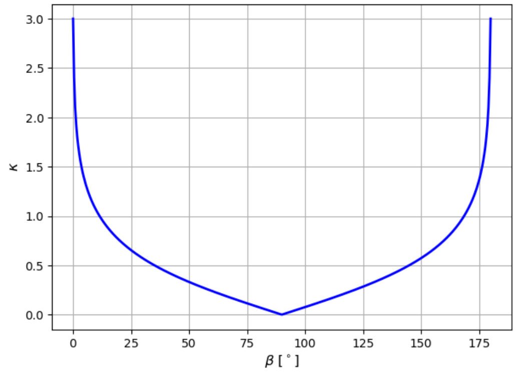

(a)

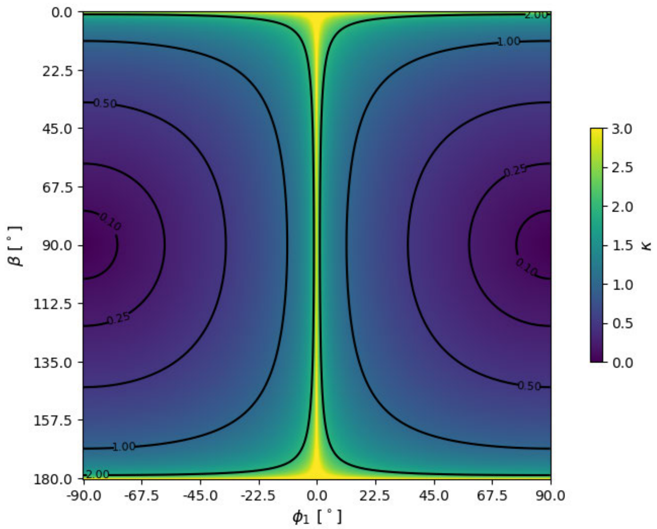

(b)

Fig. 12. Precision loss plots. (a) Precision loss variation with β when both LOSs are contained in the topographic plane (2-D case). (b) Precision loss dependence of β and φ_1 when LOS plane and topographic plane differ (3-D case).

that $s_3 = 0$ together with $n_3 = n_z = 1$. Therefore, the condition matrix for the system only depends on one geometrical parameter, the bistatic angle

$$A = \begin{bmatrix} 1 & 0 \\ \cos(\beta) & \sin(\beta) \end{bmatrix}. \tag{34}$$

Fig. 12(a) shows the variation of precision with β for the scenario just described. It can be observed that the symmetric nature of the plot around $\beta = 90°$, point at which no precision loss occurs. As expected, when both LOSs are collinear ($\beta = 0°$ or $180°$), the precision loss tends to infinity. A limit precision loss value can be set at $\kappa = 1$, meaning that the output errors will be at most ten times those at the input. In such conditions, the minimum acceptable bistatic angle of about 11.31°. In other words, radar geometries that allow bistatic angles above 11.31° will present low to moderate risk in amplification of the error. In contrast, those below 11.31° will suffer from high numerical instability.

The same approach can be followed to analyze a case with varying topography, like in this study. First, the local topography vector can be rewritten as follows:

$$n_1 = \cos(\varphi_1)\cos(\varphi_2) \tag{35}$$

$$n_2 = \cos(\varphi_1)\sin(\varphi_2) \tag{36}$$

$$n_3 = \sin(\varphi_1) \tag{37}$$

where φ_1 and φ_2 are two Euler angles, with respect to the horizontal axis and the $\hat{e}_1$-axis, respectively. If we substitute the above expressions in (19), we have that the condition matrix can be expressed as

$$A = \begin{bmatrix} 1 & 0 & 0 \\ \cos(\beta) & \sin(\beta) & 0 \\ \cos(\varphi_1)\cos(\varphi_2) & \cos(\varphi_1)\sin(\varphi_2) & \sin(\varphi_1) \end{bmatrix} \tag{38}$$

depending on three different angles expressing three DOFs. The condition number is dominated by β and φ_1, given that these two angles appear in its determinant $|A| = \sin(\beta)\sin(\varphi_1)$ and have a direct impact on the calculation of the spectral norm of order 2, as it relies on the value of the maximum eigenvalue. Fig. 12(a) shows the dependence of the condition number on the first of these two geometrical parameters. The image shows a twofold symmetry, just as the one in Fig. 12(b), with an axis of symmetry for $\beta = 90°$, and another for $\varphi_1 = 0°$. The latter means that the problem is ill-conditioned if the normal topographic vector is contained in the LOS plane. Therefore, the optimal regions exist for $\varphi_1 = \pm 90°$. If limiting again the maximum output error to ten times the one at the input, the points fulfilling that condition are enclosed within $\kappa = 1$. In the case of this study, the regions yielding a higher precision loss are the far range ($\beta \to 0°$) and steep areas ($\varphi_1 \to \pm 90°$). In most of the scenes, both conditions do not occur simultaneously; in fact, on the glacier, the topography can be assumed to be mostly flat. Therefore, the limiting β is only slightly above the 2-D case. In contrast, very steep regions ($\varphi_1 \to 0°$) quickly fall outside the locus of points of $\kappa = 1$ even for high β. This means that for our specific study area, far-range steep-sloped regions present extremely high numerical instability, which is in accordance with our findings.

VII. Conclusion

In this study, we have presented and compared two different approaches using differential interferometry and an external DEM to reconstruct the displacements of a glacier in the 3-D space. A purely monostatic approach that takes the gradient of the DEM topography as direction for the glacier motion is referred to as magnitudes uncoupled from displacements. A monostatic–bistatic approach that combines the differential interferometric data from both devices' LOS and utilizes the external DEM to restrict the solution of the plane tangent to the topography, meaning that magnitudes and displacements are coupled.

Each approach has its own particularities summarized as follows. The monostatic approach is advantageous for its single-device setup when it is reasonable to assume the direction of the displacements. In this configuration, the uncertainty of the displacement's magnitude can be considered independent of range thanks to the very high SNR throughout the whole scene. Therefore, the sources of high uncertainty are linked to unfavorable geometrical configurations between the primary's LOS direction and the gradient of the topography, which can be minimized by carefully selecting the location. For this particular case study, such critical regions correspond to high-steep areas, colored red in the digit precision loss plots. The uncoupling between the displacement's direction and magnitude causes mismatches between the two datasets, which eventually yield a more heterogeneous displacement heatmap and discontinuous vector field. The monostatic–bistatic approach requires a more complex radar setup but has the advantage of obtaining both magnitude and direction from radar measurements, using an external DEM only for an additional restriction in the geometry. This approach suffers from low SNR, particularly in far range, causing a sharp increase in uncertainty values beyond the mid-range regions. Furthermore, it affects negatively the coherence, decreasing it, and therefore, reducing the final number of available data points. Thus, there is an overall decrease in the quality of the dataset. However, the main advantage of coupling the magnitude and direction of displacements is a more robust calculation of the directions and smoother vector field.

The aim of this study has been to further explore the particularities of radar bistatic investigations, namely its different configuration geometries and how these affect the reconstruction of the displacements. Using the Aletsch Glacier as a test site together with the wide range of bistatic angles in the scene, it serves as a good proxy for future bistatic radar missions. In fact, new scientific interest is increasing for the use of systems with bistatic capabilities despite its overall contribution to radar research being rather marginal. At the moment, only one space radar mission uses a bistatic configuration (TanDEM-X [5]) and with a very limited bistatic angle (below 1°). However, upcoming bistatic missions such as Harmony [23] might reverse this trend, as they will require to work on a more diverse range of bistatic angles. In this context, KAPRI's monostatic and monostatic–bistatic displacement estimations offer a wide range of bistatic angles, a better understanding of how the SNR affects the displacement uncertainty, and a side-by-side comparison to the monostatic-only case. Therefore, this case study can prove relevant for future space missions and the advancement of bistatic radar research as a whole.

Acknowledgment

The authors would like to thank the International Foundation High Altitude Research Stations Jungfraujoch and Gornergrat (HFSJG), Bern, Switzerland, for enabling them to carry out their experiments at the Jungfraujoch High Altitude Research Station. They would also like to thank the custodians Daniela Bissig, Erich Furrer, and Christine and Ruedi Käser for the support of their activities, Philipp Bernhard and Michael Arnold for their invaluable support during campaigns, and Othmar Frey, Silvan Leinss, and Charles Werner for their technical support regarding radar operation. Map underlay: Landeskarte 1:25 000, Federal Office of Topography Swisstopo.

References

[1] A. Moreira, P. Prats-Iraola, M. Younis, G. Krieger, I. Hajnsek, and K. P. Papathanassiou, "A tutorial on synthetic aperture radar," *IEEE Geosci. Remote Sens. Mag.*, vol. 1, no. 1, pp. 6–43, Mar. 2013.

[2] D. Massonnet et al., "The displacement field of the landers earthquake mapped by radar interferometry," *Nature*, vol. 364, no. 6433, pp. 138–142, Jul. 1993. [Online]. Available: https://www.nature.com/articles/364138a0

[3] E. Rignot, K. C. Jezek, and H. G. Sohn, "Ice flow dynamics of the Greenland ice sheet from SAR interferometry," *Geophys. Res. Lett.*, vol. 22, no. 5, pp. 575–578, Mar. 1995. [Online]. Available: https://onlinelibrary.wiley.com/doi/full/10.1029/94GL03381

[4] L. C. Morena, K. V. James, and J. Beck, "An introduction to the RADARSAT-2 mission," *Can. J. Remote Sens.*, vol. 30, no. 3, pp. 221–234, Jan. 2004. [Online]. Available: https://www.tandfonline.com/doi/abs/10.5589/m04-004

[5] M. Zink, H. Fiedler, I. Hajnsek, G. Krieger, A. Moreira, and M. Werner, "The TanDEM-X mission concept," in *Proc. Int. Geosci. Remote Sens. Symp. (IGARSS)*, Jul. 2006, pp. 1938–1941.

[6] M. Pieraccini and L. Miccinesi, "Ground-based radar interferometry: A bibliographic review," *Remote Sens.*, vol. 11, no. 9, p. 1029, Apr. 2019. [Online]. Available: https://www.mdpi.com/2072-4292/11/9/1029/htm

[7] L. Pipia et al., "Polarimetric differential SAR interferometry: First results with ground-based measurements," *IEEE Geosci. Remote Sens. Lett.*, vol. 6, no. 1, pp. 167–171, Jan. 2009.

[8] D. Tarchi et al., "Landslide monitoring by using ground-based SAR interferometry: An example of application to the tessina landslide in Italy," *Eng. Geol.*, vol. 68, nos. 1–2, pp. 15–30, Feb. 2003.

[9] T. Zeng, C. Mao, C. Hu, X. Yang, and W. Tian, "Multi-static MIMO-SAR three dimensional deformation measurement system," in *Proc. IEEE 5th Asia Pacific Conf. Synth. Aperture Radar (APSAR)*, pp. 297–301, Oct. 2015.

[10] D. Voytenko et al., "Acquisition of a 3 min, two-dimensional glacier velocity field with terrestrial radar interferometry," *J. Glaciol.*, vol. 63, no. 240, pp. 629–636, Aug. 2017. [Online]. Available: https://www.org/core/journals/journal-of-glaciology/article/acquisition-of-a-3-min-twodimensional-glacier-velocity-field-with-terrestrial-radar-interferometry/8AC2AE0606B16DE3C79B5C9A3A92080E

[11] N. J. Willis, *Bistatic Radar*. London, U.K.: The Institution of Engineering and Technology (IET), 2004, doi: 10.1049/SBRA003E.

[12] M. Pieraccini, L. Miccinesi, and N. Rojhani, "A GBSAR operating in monostatic and bistatic modalities for retrieving the displacement vector," *IEEE Geosci. Remote Sens. Lett.*, vol. 14, no. 9, pp. 1494–1498, Sep. 2017. [Online]. Available: https://www.semanticscholar.org/paper/6f2e72f910bfe27b08d5821fee7ffc66d059f698

[13] L. Miccinesi and M. Pieraccini, "Monostatic/bistatic interferometric radar for monitoring slander structures," in *Proc. IEEE Conf. Antenna Meas. Appl. (CAMA)*, Oct. 2019, pp. 1–4.

[14] A. Monti-Guarnieri, P. Falcone, D. D'Aria, and G. Giunta, "3D vibration estimation from ground-based radar," *Remote Sens.*, vol. 10, no. 11, p. 1670, Oct. 2018. [Online]. Available: https://www.mdpi.com/2072-4292/10/11/1670/htm

[15] Y. Deng, C. Hu, W. Tian, and Z. Zhao, "3-D deformation measurement based on three GB-MIMO radar systems: Experimental verification and accuracy analysis," *IEEE Geosci. Remote Sens. Lett.*, vol. 18, no. 12, pp. 2092–2096, Dec. 2021.

[16] Y. Xiong, Y. Gou, W. Tian, X. Dong, G. Meng, and Z. Peng, "Full-field 3D displacement measurement via microwave sensing," *Mech. Syst. Signal Process.*, vol. 234, Jul. 2025, Art. no. 112804. [Online]. Available: https://www.sciencedirect.com/science/article/pii/S0888327025005059

[17] M. Zhang, P. Huang, Y. Qi, W. Tan, and Z. Zhang, "Retrieving the true 3D displacement of the scene based on multiple ground-based microdeformation monitoring radars," in *Proc. Photon. Electromagn. Res. Symp. (PIERS)*, Nov. 2021, pp. 2265–2272.

[18] L. Miccinesi and M. Pieraccini, "Bridge monitoring by a monostatic/bistatic interferometric radar able to retrieve the dynamic 3D displacement vector," *IEEE Access*, vol. 8, pp. 210339–210346, 2020. [Online]. Available: https://www.semanticscholar.org/paper/7992dbdc1ceee8a47955051eeb476d49c338939a

[19] L. Miccinesi, A. Beni, and M. Pieraccini, "Multi-monostatic interferometric radar for bridge monitoring," *Electronics*, vol. 10, no. 3, p. 247, Jan. 2021. [Online]. Available: https://www.mdpi.com/2079-9292/10/3/247/htm

[20] D. G. Vaughan et al., *Observations: Cryosphere*. Cambridge, U.K.: Cambridge Univ. Press, 2014, pp. 317–382.

[21] A. Moreira et al., “Tandem-L: A highly innovative bistatic SAR mission for global observation of dynamic processes on the Earth’s surface,” *IEEE Geosci. Remote Sens. Mag.*, vol. 3, no. 2, pp. 8–23, Jun. 2015. [Online]. Available: https://www.semanticscholar.org/paper/ef4c2ce7246a91016ed3b266bdb9e89ecc14cd15

[22] K. Scipal and M. Davidson, “The SAOCOM-CS mission: ESA’s first bistatic and tomographic L-band mission,” in *Proc. IEEE Int. Geosci. Remote Sens. Symp. (IGARSS)*, Jul. 2017, pp. 123–124.

[23] P. López-Dekker et al., “The harmony mission: End of phase-0 science overview,” in *Proc. IEEE Int. Geosci. Remote Sens. Symp. (IGARSS)*, Jul. 2021, pp. 7752–7755.

[24] M. Stefko, S. Leinss, O. Frey, and I. Hajnsek, “Coherent backscatter enhancement in bistatic Ku- and X-band radar observations of dry snow,” *Cryosphere*, vol. 16, no. 7, pp. 2859–2879, Jul. 2022.

[25] A.-L. Billabert, E. Pottier, and J. Saillard, “Bistatic radar polarimetry theory,” in *Bistatic Radar*, N. J. Willis and H. D. Griffiths, Eds., London, U.K.: Institution of Engineering and Technology, 2007, ch. 14, doi: 10.1201/9781420037296.ch14.

[26] K. E. Mattar, P. W. Vachon, D. Geudtner, A. L. Gray, I. G. Cumming, and M. Brugman, “Validation of Alpine glacier velocity measurements using ERS tandem-mission SAR data,” *IEEE Trans. Geosci. Remote Sens.*, vol. 36, no. 3, pp. 974–984, May 1998.

[27] P. Di Tommaso, M. Chatzou, E. W. Floden, P. P. Barja, E. Palumbo, and C. Notredame, “Nextflow enables reproducible computational workflows,” *Nature Biotechnol.*, vol. 35, no. 4, pp. 316–319, Apr. 2017. [Online]. Available: https://www.nature.com/articles/nbt.3820

[28] R. M. Goldstein and C. L. Werner, “Radar interferogram filtering for geophysical applications,” *Geophys. Res. Lett.*, vol. 25, no. 21, pp. 4035–4038, Nov. 1998. [Online]. Available: https://onlinelibrary.wiley.com/doi/full/10.1029/1998GL900033

[29] M. Stefko, P. Bernhard, O. Frey, and I. Hajnsek, “Polarimetric analysis of biseasonal monostatic and bistatic radar observations of a glacier accumulation zone at Ku-band,” *IEEE J. Sel. Topics Appl. Earth Observ. Remote Sens.*, vol. 17, pp. 9706–9727, 2024.

[30] S. V. Gupta, “Measurement uncertainties: Physical parameters and calibration of instruments,” *Meas. Uncertainties, Phys. Parameters Calibration Instrum.*, vol. 2012, pp. 1–321, Jan. 2012.

[31] C. Werner, A. Wiesmann, T. Strozzi, A. Kos, R. Caduff, and U. Wegmiüler, “The GPRI multi-mode differential interferometric radar for ground-based observations,” in *Proc. 9th Eur. Conf. Synth. Aperture Radar (EUSAR)*, Apr. 2012, pp. 304–307.

[32] J. Dainty, *Laser Speckle and Related Phenomenon*. Berlin, Germany: Springer, 1984.

[33] L. N. Trefethen and D. Bau, *Numerical Linear Algebra*. Philadelphia, PA, USA: SIAM, 2022.

[34] K. Atkinson, *An Introduction to Numerical Analysis*. Hoboken, NJ, USA: Wiley, 1991.

[35] G. Strang, *Linear Algebra and its Applications*. Orlando, FL, USA: Academic, 1980.

[36] C. Werner, T. Strozzi, A. Wiesmann, and U. Wegmuller, “A real-aperture radar for ground-based differential interferometry,” in *Proc. IEEE Int. Geosci. Remote Sens. Symp. (IGARSS)*, Jul. 2008, vol. 3, no. 1, pp. 210–213.

[37] S. Baffelli, O. Frey, C. Werner, and I. Hajnsek, “Polarimetric calibration of the Ku-band advanced polarimetric radar interferometer,” *IEEE Trans. Geosci. Remote Sens.*, vol. 56, no. 4, pp. 2295–2311, Apr. 2018.

[38] M. Stefko, O. Frey, C. Werner, and I. Hajnsek, “Calibration and operation of a bistatic real-aperture polarimetric-interferometric Ku-band radar,” *IEEE Trans. Geosci. Remote Sens.*, vol. 60, 2022, Art. no. 5106719, doi: 10.1109/TGRS.2021.3121466.

[39] T. Strozzi, C. Werner, A. Wiesmann, and U. Wegmuller, “Topography mapping with a portable real-aperture radar interferometer,” *IEEE Geosci. Remote Sens. Lett.*, vol. 9, no. 2, pp. 277–281, Mar. 2012.

[40] GAMMA Remote Sens. AG. (2023). *GAMMA Portable Radar Interferometer Model: GPRI-II User Manual*. [Online]. Available: https://www.gamma-rs.ch

[41] E. Mas Sanz, M. Stefko, and I. Hajnsek, “Digital elevation model estimation and recovery of displacements over the great aletsch glacier,” in *Proc. 15th Eur. Conf. Synth. Aperture Radar (EUSAR)*, Apr. 2024, pp. 191–196.

Esther Mas Sanz (Member, IEEE) received the joint M.Sc. degree in cold climate engineering from the Technical University of Denmark (DTU), Kongens Lyngby, Denmark, and the Norwegian University of Science and Technology (NTNU), Trondheim, Norway, in 2022, and the M.Sc. degree in aerospace engineering from the Polytechnic University of Catalonia (UPC), Terrassa, Spain, in 2018. She is currently pursuing the Ph.D. degree with ETH Zürich, Zürich, Switzerland, focusing on the applications and analysis of bistatic radar signals in cryospheric environments.

Her research involves developing data pipelines, radar image processing, and the organization and logistics of fieldwork campaigns in the Alps.

Marcel Stefko (Member, IEEE) received the M.Sc. degree in applied physics from the École Polytechnique Fédérale de Lausanne (EPFL), Lausanne, Switzerland, in 2017, and the Ph.D. (Dr.Sc.) degree in radar remote sensing from ETH Zürich, Zürich, Switzerland, in 2023.

From 2017 to 2018, he was a Young Graduate Trainee with European Space Agency, Noordwijk, The Netherlands. He is currently with the Chair of Earth Observation and Remote Sensing, ETH Zürich. His Ph.D. work focused on the development of calibration, data acquisition, and data processing methods for bistatic radar systems, and the exploration of potential applications of these systems in natural environments. His research focuses on the exploitation of bistatic radar systems for monitoring of snow-covered environments.

Irena Hajnsek (Fellow, IEEE) received the Diploma degree (Hons.) in fluvial river systems from the Free University of Berlin, Berlin, Germany, in 1996, and the Dr.rer.nat. degree (Hons.) from Friedrich Schiller University Jena, Jena, Germany, in 2001, with a focus on model-based estimation of soil moisture from fully polarimetric synthetic aperture radar.

Since 2009, she has been a Professor of Earth observation with the Institute of Environmental Engineering, Swiss Federal Institute of Technology (ETH), Zürich, Switzerland, and the Head of the Polarimetric SAR Interferometry Research Group, Microwaves and Radar Institute, German Aerospace Center, Köln, Germany. Since 2010, she has been the Science Coordinator at German satellite mission TanDEM-X. Her research interests include electromagnetic propagation and scattering theory, radar polarimetry, synthetic aperture radar (SAR) and interferometric SAR data processing techniques, and environmental parameter modeling and estimation.

Dr. Hajnsek was a member of the IEEE GRSS AdCom from 2013 to 2021. She is a member of European Space Agency Mission Advisory Group for the ROSE-L Mission. She was the Technical Program Co-Chair of the IEEE IGARSS 2012 in Munich, Germany, and in Yokohama, Japan, in 2019. From 2016 to 2020, she was the Vice President of the IEEE GRSS Technical Committees. She is the Founder of the new Technical Committee Remote Sensing Environment, Analysis and Climate Technologies (REACT) that exists since November 2021.